# Gamow-Teller strength from the $^{20}$Ne$(n,p)^{20}$F reaction at $E_n = 198$ MeV

B. W. Pointon,[1,*] O. Häusser,[1,2] R. Henderson,[2] A. Celler,[3] K. Hicks,[2,†] K. P. Jackson,[2] R. Jeppesen,[1,‡] B. Larson,[1] J. Mildenberger,[1,§] A. Trudel,[1] M. Vetterli,[2] and S. Yen[2]

[1]*Simon Fraser University, Burnaby, British Columbia, Canada V5A 1S6*

[2]*TRIUMF 4004 Wesbrook Mall, Vancouver, British Columbia, Canada V6T 2A3*

[3]*University of Western Ontario, London, Ontario, Canada N6A 3K7*

(Received 13 August 1991)

Cross sections for the $^{20}$Ne$(n,p)^{20}$F reaction at $E_n = 198$ MeV were measured at five angles using the TRIUMF charge-exchange facility and a novel high-pressure (20 atm, or 2.03 MPa) gas target. The $L=0$, $L=1$, and $L \geq 2$ contributions to the cross sections were obtained from a multipole decomposition. Using an empirical proportionality between the cross section and Gamow-Teller (GT) strength from $\beta$ decay, GT strength was deduced up to an excitation of 10 MeV in $^{20}$F. Most of the strength is concentrated in a discrete state at $E_x = 1.0$ MeV, with the extracted strength of the $\Delta L=0$ continuum at high excitation having a large error. These results are compared with measurements of GT strength using other probes. Comparison with the measured magnetic dipole ($M1$) strength in $^{20}$Ne shows that there is constructive interference between the spin part and a large orbital part of the $M1$ transition to the 11.26 MeV state in $^{20}$Ne (analog of the 1.0 MeV state in $^{20}$F). If all the strength from the multipole decomposition is used, we find agreement of the total GT strength compared to untruncated *sd* shell-model calculations which use free-nucleon operators, although experimental and theoretical distributions differ in detail. The confirmation of strong orbital $M1$ contributions at the beginning of the *sd* shell together with systematics of GT quenching in heavier *sd* shell nuclei may provide evidence for meson exchange currents in $M1$ transitions.

## I. INTRODUCTION

In the last decade there has been renewed interest in Gamow-Teller (GT) strength distributions in nuclei. Because of the simple form of the GT one-body transition operator, GT transitions provide a simple, straightforward testing ground for current models of nuclear structure. Also, the empirical proportionality between nucleon charge-exchange reaction cross sections at intermediate energies and GT strength in $\beta$ decay [1,2] has expanded the energy range over which GT strength can be compared to theoretical models. The total GT strength summed over a wide range of excitation in the final nucleus provides new tests of shell-model truncation effects and of possible excited nucleon configurations ($\Delta$ isobar components) in the nucleus [3,4].

GT strength distributions in the *sd* shell are of special interest because reliable nucleonic wave functions are available from shell-model calculations [5] using a sophisticated, fine-tuned two-body interaction and unrestricted configuration mixing within the full *sd* valence shell. The shell-model wave functions have been extensively tested against experimental data on binding and excitation energies, static moments, electromagnetic transitions, and spectroscopic factors in nucleon transfer reactions [6,7]. A comparison of GT and $M1$ one-body operators is particularly fruitful since the nucleonic spin part of the matrix elements, $M(\sigma)$, provides the largest contributions to both. For $0^+$, $T=0 \rightarrow 1^+$, $T=1$ analog transitions the GT and $M1$ strengths can be written [3,6]

$$B(M1) = \frac{3(\mu_p - \mu_n)^2}{8\pi}[M(\sigma) + M(l) + M_\Delta + M_V^{\mathrm{MEC}}]^2,$$

$$B(GT) = [M(\sigma) + M_\Delta + M_A^{\mathrm{MEC}}]^2 ,$$

where the numerical factor in the $B(M1)$ expression is $2.643\mu_N^2$, and the ratio of coupling constants, $(g_A/g_V)^2$, is not included in the definition of $B(GT)$. The nucleonic spin matrix elements $M(\sigma)$ and the isobar contributions $M_\Delta$ are the same in both expressions. The meson-exchange-current (MEC) contributions are dominated by pion exchange and are predicted [3] to be large for isovector $M1$ currents. They are strongly suppressed for axial-vector (GT) currents because of conservation of $G$ parity. From a comparison of GT and $M1$ strengths the combined effects of orbital and MEC contributions can be seen. In their absence the ratio $R(M1/\mathrm{GT}) = [\sum B(M1)/2.643\mu_N^2]/\sum B(\mathrm{GT})$ is unity, irrespective of the complexity of the nucleonic wave functions, and of the exact magnitude of delta isobar contributions. Systematics of theoretical GT and $M1$ strength across the *sd* shell [6] show that MEC's are a consistently large effect in $M1$ transitions whereas orbital contributions are expected to be large at the beginning of the *sd* shell, and of lesser importance in the middle and upper half.

A reliable measurement of the interference between $M(\sigma)$ and $M(l)$ is needed at the beginning of the *sd* shell where $M(l)$ is expected to be large. We have studied the $^{20}$Ne$(n,p)^{20}$F reaction at 198 MeV primarily to measure the GT distribution in $^{20}$F in comparison with $M1$

 

strength in $^{20}$Ne from $(e,e')$ [8] and $(\gamma,\gamma')$ [9,10] reactions. The present work is complementary to recent measurements of GT strength to $1^+$, $T=1$ analog states (i) in $^{20}$Ne by the $(p,p')$ [11], (ii) in $^{20}$F by the $(\pi^-,\gamma)$ [12], and (iii) in $^{20}$Na by the $(p,n)$ [13] reaction. The $(p,p')$ and $(\pi^-,\gamma)$ studies were unable to measure the total GT strength because of limitations in the signal to background ratio. Furthermore, angular distributions from $(p,p')$ reactions cannot easily distinguish between isospin $T=0$ and $T=1$ of the final states [$T=0$ states in $(e,e')$ are highly suppressed]. Both $(n,p)$ and $(p,n)$ reactions at intermediate energies are reliable probes of GT strength. For $N=Z$ isoscalar target nuclei, because of approximate charge symmetry of nuclear forces, these reactions are largely equivalent. The $(n,p)$ work described in the following sections was carried out at TRIUMF's charge-exchange (CHARGEX) facility [14] and was the first experiment to utilize the high-pressure gas target [15] developed for this facility.

## II. EXPERIMENTAL METHOD

The $^{20}$Ne$(n,p)^{20}$F reaction at $E_n=198$ MeV was measured at five scattering angles using the CHARGEX facility in the $(n,p)$ mode [14]. In this setup which is shown schematically in Fig. 1 a nearly monoenergetic neutron beam of 198 MeV was produced by the $^7$Li$(p,n)^7$Be reaction populating the doublet of ground state and first excited state (427 keV) in $^7$Be. The neutron beam with a typical flux of $10^5$ s$^{-1}$ cm$^{-2}$ contains a weak (about 1%/MeV) tail associated with the $^7$Be continuum response. A compact magnet immediately downstream of the primary target deflected the proton beam by 20° into a shielded beam dump. Neutrons from the $^7$Li$(p,n)^7$Be reaction interacted with the segmented $(n,p)$ target contained in a target box 93 cm downstream of the primary target. A thin scintillation counter ($VS$) in front of the target box was used to discriminate against incoming charged particles.

The $(n,p)$ gas target was specifically designed for the present experiment and is described in detail elsewhere [15]. The Ne gas, isotopically enriched to 99.95% in $^{20}$Ne and at a pressure of 20 atm, was contained in two separate cells to allow for energy loss corrections within the thick total target. The $^{20}$Ne areal density was 66.3 mg/cm$^2$ per cell. Stainless-steel windows, 25 $\mu$m thick in initial runs, 5 $\mu$m thick for later runs, separated the isotopic gas from counter gas (90% Ar, 10% $CO_2$). The counter gas was at a slightly lower pressure than 20 atm to maintain a convex curvature of the windows. Two solid targets of 44-mg/cm$^2$-thick $CH_2$ were mounted upstream and downstream of the gas target cells to normalize the $^{20}$Ne$(n,p)$ reaction yields relative to those of the H$(n,p)$ reaction for which absolute cross sections are known. Protons originating either in one of the gas cells or in one of the two $CH_2$ targets were identified from the hit pattern of the wire chambers labeled $Y_{V'}$, $Y_A$, $Y_B$, $Y_C$, and $Y_D$ in Fig. 1. $Y_{V'}$, the first of the wire chambers, served as an additional charged-particle veto. The efficiencies of the wire chambers (typically 99%) were measured in separate runs using protons produced by the H$(n,p)$ reaction in a thick block of $CH_2$ placed in front of the $(n,p)$ target box.

Protons from the $(n,p)$ reaction were momentum analyzed by the medium resolution spectrometer (MRS) consisting of a quadrupole-dipole system [16]. Two sets of front end chambers (FECM and FEC0 in Fig. 1) between target box and MRS quadrupole allow ray tracing of the protons to the origin of the $(n,p)$ reaction. Valid events require the horizontal vertex positions derived from the $YM/Y0$ and from the $Y_A-Y_D$ wire chamber information

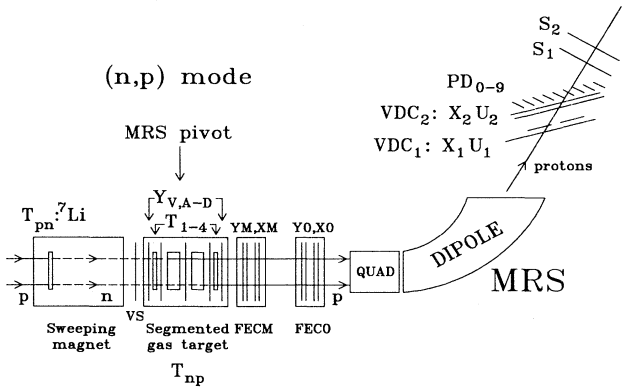


FIG. 1. Schematic layout of the TRIUMF charge-exchange facility in the $(n,p)$ configuration for gas targets.

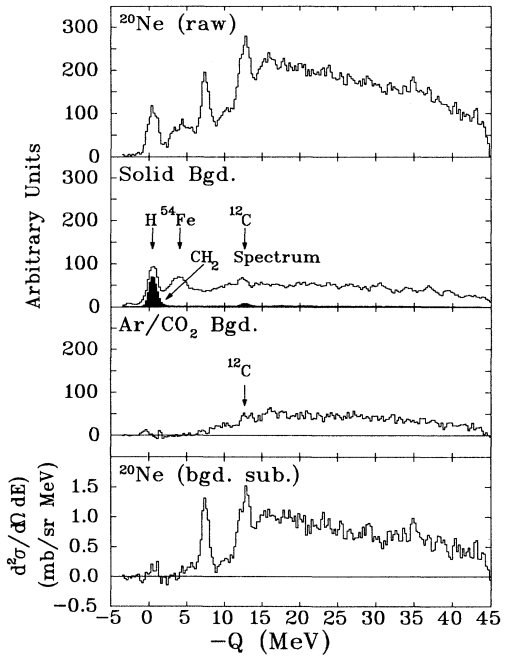


FIG. 2. The raw $^{20}$Ne$(n,p)^{20}$F spectrum at $E_n=198$ MeV is shown on the top. The second and third panels show the normalized backgrounds from chamber gas and solids. The bottom panel shows the background corrected $^{20}$Ne$(n,p)^{20}$F spectrum roughly in units of cross section per MeV.

to agree to within a few mm. Spectra were measured with the MRS at nominal positions of 0°, 3°, 6°, 10°, and 15°. The corresponding average laboratory scattering angles were measured to be 1.53°, 3.3°, 6.63°, 10.3°, and 15.3°, respectively.

In addition to the $^{20}$Ne$(n,p)$ measurements, additional runs were necessary to determine the background contributions to the proton spectra (see Fig. 2). At each MRS angle, data were taken with Ar/$CO_2$ counter gas in the cells at both 20 and 1 atm. The background subtraction will be discussed below (see also Ref. [15]) and is illustrated by the series of spectra in Fig. 2.

Neutron beam energy spread, energy loss in one of the $^{20}$Ne gas cells and in the cell window, and energy loss and angular straggling in the 0.5-mm-thick target box exit window are the major contributors to the energy resolution in the $(n,p)$ spectra. Since the effects of angular straggling in the exit window increase with increasing MRS angle, the energy resolution was angle dependent, varying from 1.1 MeV FWHM at 0° to about 2.3 MeV FWHM at 15°.

## III. DATA ANALYSIS

The data analysis procedures adopted for the present experiment are similar to those described in detail in previous publications of TRIUMF $(n,p)$ work [17–20]. Only the most important steps will be discussed here.

First, normalized raw momentum spectra were obtained for events which satisfied the criteria for good wire chamber positions including traceback to the target, and appropriate cuts in the energy and time-of-flight spectra for the MRS trigger scintillators. After identifying the origin of the $(n,p)$ reaction from the $Y_A - Y_D$ wire chamber information "target gas" and "$CH_2$" spectra were obtained. These spectra were corrected for wire chamber inefficiencies (about 1% per plane) using a straightforward procedure described elsewhere [18,19].

The raw spectra are then corrected for background from $(n,p)$ conversions in the counter gas and in solid materials (stainless-steel windows and wire chamber anodes and cathode foils). The "counter gas background" spectrum is a factor of $\frac{20}{19}$ times the difference of the 20 and 1 atm spectra measured with Ar/$CO_2$ in the gas target cells. This spectrum is then normalized by the fractional length of the counter gas outside the target cells. The "solid background" spectrum is obtained from the 1 atm spectrum by subtraction of $\frac{1}{20}$th of the "counter gas background." At the start of this procedure the energy resolution of the 1 atm spectra was artificially broadened to equal that of the 20 atm spectra.

The background corrected "target gas" spectra are then corrected for the variation of the MRS acceptance versus focal plane position. The MRS acceptance function had been determined empirically by measuring the yield for the H$(n,p)$ reaction at different field settings of the MRS dipole. The acceptance correction is most important at the low-momentum, high excitation energy end of the spectra.

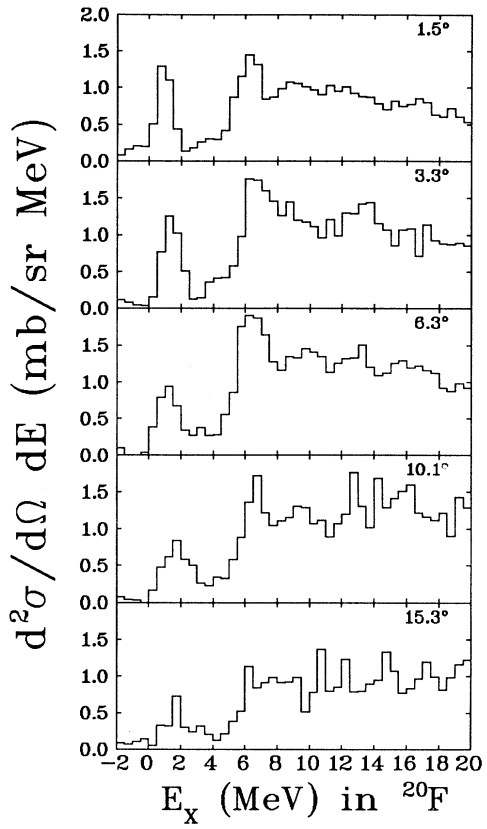


FIG. 3. The $^{20}$Ne$(n,p)^{20}$F cross sections at $E_n = 198$ MeV, using 0.5 MeV bins. The average laboratory scattering angles are 1.53°, 3.3°, 6.63°, 10.3°, and 15.3°.

TABLE I. Nominal MRS angle, corresponding average laboratory and center-of-mass angles, and laboratory cross sections for the H$(n,p)$ reaction at 198 MeV [21].

| Nominal MRS angle in lab | Average MRS angle in lab | Average MRS angle in c.m.s. | H$(n,p)_{lab}$ cross section (mb/sr) |
|---|---|---|---|
| 0.0 | 1.53 | 1.63 | 53.53 |
| 3.0 | 3.34 | 3.54 | 48.20 |
| 6.0 | 6.30 | 6.68 | 40.18 |
| 10.0 | 10.11 | 10.72 | 31.28 |
| 15.0 | 15.3 | 16.22 | 24.56 |

The energy spectra for the H$(n,p)$ reaction exhibit a 198 MeV peak from the $^7$Be ground and first excited state and a low-momentum tail from the $^7$Be continuum. The contribution of the low-momentum tail in the incident neutron spectrum to the "target gas" spectra was removed by a simple deconvolution procedure.

Final "$^{20}$Ne" and "$CH_2$" spectra were sorted into energy bins after correcting for the different energy losses due to reaction origins in different sections of the target box. The "$^{20}$Ne" spectra were converted to units of cross section per MeV by normalizing to the prominent H$(n,p)$ peak in the "$CH_2$" spectra for which the cross sections were inferred from the SAID phase-shift solutions [21]. The average laboratory and center-of-mass angles and the H$(n,p)$ cross sections for the five MRS angle settings are given in Table I. The "$^{20}$Ne" cross sections were then converted to the center of mass for comparison with theory. These final, normalized center-of-mass spectra are shown in Fig. 3.

## IV. RESULTS

The forward-angle spectra in Fig. 3 show two peaks, at 1.0 MeV and at 6.5 MeV, and only hints of other structure. The angular distributions suggest that both peaks have contributions from both $\Delta L=0$ and $\Delta L=1$ transitions. The 1.0 MeV peak is relatively free of background at each angle, whereas the 6.5 MeV peak is superimposed on a large background, making a reliable, quantitative analysis difficult. A multipole decomposition [22] was carried out for the energy distributions up to $E_x=10$ MeV in $^{20}$F, with a separate analysis of the angular distribution for the isolated 1.0 MeV peak.

For this analysis theoretical angular distributions were calculated with the distorted-wave-impulse approximation (DWIA) using the code DW81 [23]. The reaction calculations used the nonrelativistic effective interaction of Franey and Love derived from the SP84 nucleon-nucleon phase-shift solution [24]. Distorted waves were obtained from the optical model using potential parameters from fits to proton elastic-scattering data on $^{24}$Mg and $^{28}$Si at 200 and 280 MeV, scaled to an incident energy of 200 MeV and to mass number 20 [25].

One-body transition densities required as input for DW81 were calculated by the shell-model code OXBASH [26]. Wave functions for the $^{20}$Ne ground state and the $1^+$, $T=1$ states in $^{20}$F were calculated with the universal *sd* shell (SD) interaction of Wildenthal [5] assuming unrestricted $0\hbar\omega$ configuration mixing for the $0d_{5/2}$, $1s_{1/2}$, and $0d_{3/2}$ single-particle states. The calculated GT and $M1$ strengths are shown in Table II. The calculations used both free-nucleon operators and effective empirical operators of Brown and Wildenthal [6] which had been fitted to data from many *sd* shell nuclei.

For a decomposition of the cross sections into multipoles [22] additional angular distributions for $\Delta L=1,2$ transitions were required. Transition densities for $\Delta L=1$ transitions at $0^-$, $1^-$, and $2^-$, $T=1$ final states were calculated by Brown [27] using the Skyrme II interaction and $1\hbar\omega$ excitations in the full *s-p-sd-fp* valence shell basis. For the $\Delta L=2$ transitions to $1^+$, $2^+$, and $3^+$, $T=1$ final states we assumed simple $0\hbar\omega$ transitions within the *sd* valence shell.

### A. The 1.0 MeV excitation in $^{20}$F

Because of the limited energy resolution, the prominent peak at $E_x=1.0$ MeV may have contributions from several final states. Candidates are the $1^+$, $T=1$ state at $E_x=1.0568$ MeV in $^{20}$F, a $1^-$ state at 0.9378 MeV and two $2^-$ states, at 1.309 and 1.843 MeV [28]. These states are analogs of the $1^+$, $T=1$ states in $^{20}$Ne at 11.26, 11.270, 11.60, and 12.098 MeV, respectively. The $2^-$ states in $^{20}$Ne are clearly seen in $(p,p')$ and $(e,e')$ reactions [11,29]. The shell-model calculations place these states several MeV too high, at 15.53 and 15.83 MeV.

The cross section for the 1.0 MeV peak was obtained at each angle by fitting a skewed Gaussian shape to the peak. The angular distribution of the peak was decomposed (see Fig. 4) into a weighted sum of distributions calculated for the $\Delta L=0$ transition to the lowest and strongest $1^+$ final state (dashed line in Fig. 4), and for the

TABLE II. Gamow-Teller and $M1$ strengths of transitions to the first ten $1^+$, $T=1$ states in $^{20}$Ne, calculated using transition densities from OXBASH, and using free and effective operators.

| $E_x$ (MeV) | $B(\mathrm{GT})_{\mathrm{free}}$ | $B(\mathrm{GT})_{\mathrm{eff}}$ | $B(M1)_{\mathrm{free}}$ ($\mu_N^2$) | $B(M1)_{\mathrm{eff}}$ ($\mu_N^2$) |
|---|---|---|---|---|
| 11.196 | 0.14233 | 0.09847 | 1.95862 | 2.32307 |
| 13.496 | 0.10168 | 0.06211 | 0.03698 | 0.00319 |
| 15.030 | 0.00025 | 0.00034 | 0.02483 | 0.03714 |
| 15.359 | 0.00076 | 0.00012 | 0.00548 | 0.00018 |
| 15.863 | 0.04505 | 0.02177 | 0.05293 | 0.00497 |
| 16.639 | 0.00858 | 0.00387 | 0.05100 | 0.01854 |
| 17.114 | 0.00418 | 0.00219 | 0.00158 | 0.00821 |
| 17.269 | 0.12634 | 0.07196 | 0.00372 | 0.01041 |
| 18.705 | 0.03929 | 0.02168 | 0.02290 | 0.00211 |
| 19.266 | 0.01872 | 0.01132 | 0.17981 | 0.15944 |
| Total | 0.48728 | 0.29383 | 2.33786 | 2.56486 |

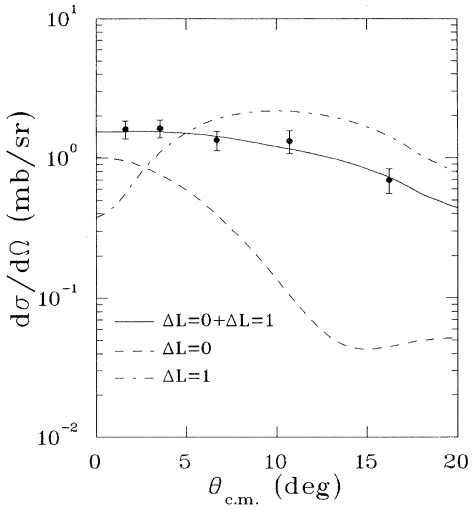


FIG. 4. The angular distribution for the $E_x = 1.0$ MeV peak in $^{20}$F. The theoretical curves are DW81 reaction calculations explained in the text.

sum of $\Delta L = 1$ transitions to the $1^-$ and $2^-$ final states mentioned above (dot-dashed line in Fig. 4). To fit the data in Fig. 4 the $\Delta L = 0$ and $\Delta L = 1$ cross sections were normalized by factors of 1.25±0.05 and 0.45±0.05, respectively (solid line). The cross section of the $\Delta L = 0$ component is then extrapolated to $\theta_{c.m.} = 0°$ using the theoretical angular distributions. The $\Delta L = 0$ cross-section contribution to the 1.0 MeV peak, extrapolated to 0°, is 1.34±0.19 mb/sr (see Table III).

### B. Multipole decomposition

A multipole decomposition of the spectra in Fig. 3 was carried out to identify distributed GT strength. In such a least-squares fitting procedure [22,18] the angular distributions for each energy bin is fitted to a sum of theoretical angular distributions of different multipolarity, convoluted with the experimental scattering angle distribution. For the present analysis only contributions from the $\Delta L = 0$, $\Delta L = 1$, and $\Delta L \geq 2$ multipoles were considered since the $^{20}$Ne$(n,p)^{20}$F spectra were only measured out to $\theta_{lab} = 15.3°$, near the peak of the $\Delta L = 2$ angular distribution.

Two sets of theoretical angular distributions were used as input, *A* and *B*. For decomposition *A* only the single strongest transition for each multipole and excitation region were used. For decomposition *B* each multipole contribution consisted of the incoherent sum of angular distributions for different final states. The $\Delta L = 0$ angular distributions included transitions to the ten lowest $1^+$, $T = 1$ states. For the $\Delta L = 1$ multipolarity the strongest final states (one $0^-$, three $1^-$, and three $2^-$) were included. The $\Delta L = 2$ multipolarity included angular distributions for the ten lowest $2^+$ and $3^+$ final states.

The results of decomposition *B* are shown in Fig. 5, with decomposition *A* giving very similar results. The decompositions indicate that the $\Delta L = 0$ strength resides largely in the two peaks at $E_x = 1.0$ and 6.5 MeV, with significant contributions from spin-dipole ($\Delta L = 1$, $\Delta T = 1$, $\Delta S = 1$) transitions. The decompositions suggest a continuum of $\Delta L = 0$ strength, significant even above 7.5 MeV, where the shell-model calculations predict very little $\Delta L = 0$ strength. The angular distributions in this excitation region are fairly flat, and the $\Delta L = 0$ contribution depends strongly on the calculated $\Delta L = 1,2$ angular distributions being correct.

Multipole decompositions of angular distributions for $^{15}$N$(n,p)^{15}$C at 290 MeV [20], for $^{54}$Fe$(n,p)^{54}$Mn at 298 MeV [18], and for $^{48}$Ti$(n,p)^{48}$Sc at 200 MeV [30] have all found distributed $\Delta L = 0$ strength at high excitation. This strength could be spurious if the calculated angular distribution shapes are incorrect and the $\Delta L = 1$ spin dipole cross sections near 0° are too small at low angles as was suggested in the $^{15}$N$(n,p)^{15}$C experiment [20]. If the distributed $\Delta L = 0$ strength is real, it is unaccounted for in the $0\hbar\omega$ shell model, but may arise from higher-order

TABLE III. Experimental cross sections, $\Delta L = 0$ components from the multipole decomposition, energy-momentum extrapolated $\Delta L = 0$ components, and final *B*(GT) values, in 1.0 MeV bins.

| $E_x$ (MeV) | $\sigma_{cm}(1.5°)$ (mb/sr) | $\sigma_{\Delta L=0}(1.5°)$ (mb/sr) | $\sigma_{q=\omega=0}$ (mb/sr) | *B*(GT) |
|---|---|---|---|---|
| 1.0 MeV peak | | 1.34±0.19 | 1.44±0.21 | 0.161±0.029 |
| 0-1 | 0.797±0.121 | 0.525±0.111 | 0.598±0.126 | 0.066±0.014 |
| 1-2 | 0.681±0.105 | 0.577±0.135 | 0.667±0.155 | 0.074±0.017 |
| 2-3 | 0.138±0.020 | 0.000±0.061 | 0.000±0.071 | 0.000±0.007 |
| 3-4 | 0.246±0.033 | 0.158±0.045 | 0.191±0.054 | 0.021±0.006 |
| 4-5 | 0.316±0.041 | 0.210±0.057 | 0.257±0.070 | 0.029±0.007 |
| 5-6 | 0.899±0.106 | 0.529±0.128 | 0.660±0.161 | 0.074±0.018 |
| 6-7 | 1.156±0.136 | 0.713±0.191 | 0.913±0.244 | 0.102±0.027 |
| 7-8 | 0.760±0.098 | 0.393±0.142 | 0.514±0.186 | 0.057±0.020 |
| 8-9 | 0.911±0.110 | 0.615±0.151 | 0.826±0.202 | 0.092±0.022 |
| 9-10 | 0.917±0.109 | 0.460±0.154 | 0.635±0.210 | 0.071±0.024 |
| Total | | | | 0.585±0.209 |

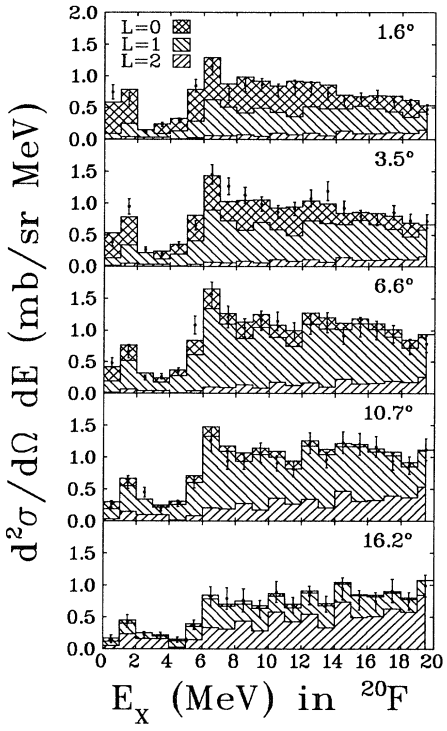


FIG. 5. The results of a multipole decomposition of the $^{20}$Ne($n$,$p$)$^{20}$F spectra at $E_n = 198$ MeV showing contributions from different $\Delta L$ components at different center-of-mass angles.

configuration mixing [31]. In the absence of extensive tests of $\Delta L = 1$ angular distributions definitive conclusions cannot be drawn from experiment at present.

### C. Gamow-Teller strength

Previous work on charge-exchange reactions has established a close proportionality between GT strength from $ft$ values in $\beta$ decay and cross sections from charge-exchange reactions extrapolated to vanishing momentum and energy transfer, $q = 0$, $\omega = 0$. The proportionality factor, or "unit cross section", $\hat{\sigma} = \sigma(q=0,\omega=0)/B(\mathrm{GT})$, depends on the mass number of the target and the incident nucleon energy. Because of uncertainties in the DWIA reaction model empirical determinations of $\hat{\sigma}$ are preferred [1]. Using a fit to a data set of 17 known $\hat{\sigma}_{\mathrm{GT}}$ values for $A$ between 6 and 54 and for energies between 135 and 492 MeV, $\hat{\sigma}_{\mathrm{GT}}$ for $A = 20$ and $E = 198$ MeV was found to be $9.0 \pm .6$ mb/sr [32]. The quoted error reflects errors of individual measurements and the spread of fitted values when adopting different subsets of the 17 data points.

The GT strength in $^{20}$F was then obtained by extrapolating the $\Delta L = 0$ contributions to the forward-angle cross sections to $\theta = 0, \omega = 0$ using the angle and energy transfer dependence indicated by DW81 calculations, and dividing them by the adopted value for $\hat{\sigma}$. The extracted GT strength from the decomposition of both the 1.0 MeV peak and the full spectrum is shown in Table III. The errors include contributions from counting statistics, from the spread in results for the multipole decompositions $A$ and $B$ and the uncertainty in the adopted value for $\hat{\sigma}$.

The experimentally extracted GT strength can then be compared with that from shell-model calculations. The measured strength of the transition to the 1.0 MeV state in $^{20}$F, $B(\mathrm{GT}) = 0.161 \pm 0.029$, is in reasonable agreement with the shell model which predicts values of 0.142 and 0.0985 using free-nucleon or effective operators, respectively. No other individual GT strength could be resolved. The strength of the transition to the 3.4 MeV state in $^{20}$F (corresponding to the 13.5 MeV state $^{20}$Ne) is calculated to be $B(\mathrm{GT}) = 0.102$ yet the strength measured at this excitation energy is only $B(\mathrm{GT}) = 0.021 \pm 0.006$. The measured strengths of transitions to states at 5.7, 7.1, and 8.5 MeV in $^{20}$F (15.9, 17.3, and 18.7 MeV in $^{20}$Ne) are also much smaller than predicted. Figure 6 compares the extracted GT strength distribution with the shell-model predictions. The measured strength distribution is not well reproduced by the calculations. Figure 7 shows the running sum of the measured $B(\mathrm{GT})$ for $E_x = 0$–$10$ MeV in $^{20}$F compared to theory. Steps in the theoretical values occur at energies where $1^+$ levels are predicted whereas those for the measured GT strength are located at the regular 1 MeV binning intervals. The comparison shows that, if the decomposition is correct, the measured GT strength summed up to an excitation energy of $E_{\max} = 10.0$ MeV is 120% of the strength predicted using free-nucleon operators.

### D. Spin-orbital interference

As already stated in the Introduction, the ratio of $M1$ and GT strengths,

$$R(M1/\mathrm{GT}) = [\textstyle\sum B(M1)/2.643\mu_n^2]/B(\mathrm{GT}) ,$$

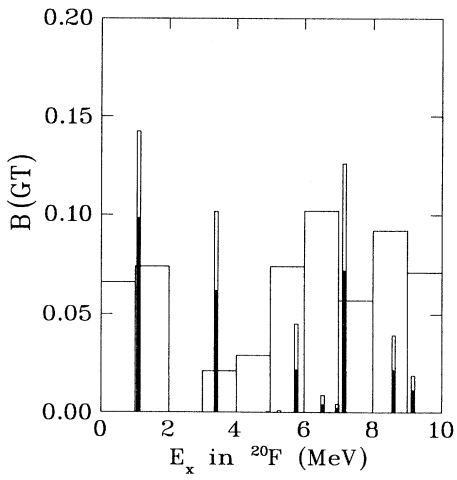


FIG. 6. The experimentally measured GT strength per MeV bin (broad bins) compared with the calculated GT strength from free-nucleon operators (narrow bins, unfilled) and effective operators (narrow bins, filled) in the $^{20}$F spectrum.

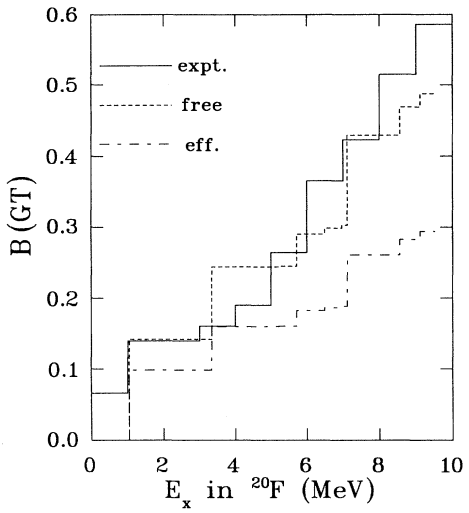


FIG. 7. The running sum of $B$(GT) versus excitation energy from the multipole decomposition of the data (solid line) and from the *sd* shell model using free-nucleon (dashed line) and effective (dot-dashed line) operators.

is a dimensionless measure of the combined effects of orbital [$M(l)$] and MEC ($M_V^{\mathrm{MEC}}$) contributions to the $M1$ matrix element, $R$ being unity in their absence. Unfortunately the individual contributions cannot be extracted from this ratio.

The $M1$ strength in $^{20}$Ne has been measured by two reactions, $(e,e')$ and $(\gamma,\gamma')$. The $(\gamma,\gamma')$ reaction is limited by the particle emission threshold to states with $E_x \leq 13.0$ MeV in $^{20}$Ne. Experiments using both probes only see the 11.26 MeV $1^+$, $T=1$ state [8,9,10] with an average strength of $B(M1)=(2.02\pm0.36)\mu_n^2$. The shell model predicts $B(M1)=1.96\mu_n^2$ using free-nucleon operators and $B(M1)=2.32\mu_n^2$ using the effective operator. Together with $B(\mathrm{GT})=0.161\pm0.029$ from the present work we find $R(M1/\mathrm{GT})=4.8\pm1.2$. This should be compared with the values 5.21 and 8.92, from calculations with free and effective one-body operators, respectively. The large experimental value for $R(M1/\mathrm{GT})$ confirms the constructive interference of large $M(l)$ and $M(\sigma)$ matrix elements for this transition as was already concluded from previous studies [11,12,13]. The experimental results are in better agreement with the free-nucleon operator predictions.

### E. Comparison with other experiments

Three other hadronic probes have been used to measure $B$(GT) in mass-20 nuclei. The earliest measurement was made using the $^{20}$Ne$(\pi^-,\gamma)^{20}$F reaction [12] which populates preferentially higher angular momentum states. The onset of nucleon emission limited the states observed in $^{20}$F to less than 7.0 MeV excitation. The 1.0 MeV state was the only $1^+$ state populated and $B(\mathrm{GT})=0.1607\pm0.030$ was obtained in good agreement with our $(n,p)$ results. A state also seen at 6.0 MeV in $^{20}$F was assigned by the authors to be $2^-$, but Rangacharyulu *et al.* [29] later suggested that this state might have a large component of $\Delta L=0$ strength.

High resolution $^{20}$Ne$(p,p')$ at low momentum transfer shows three distinct $1^+$ peaks at 11.26, 13.5, and 15.7 MeV, with strengths roughly as expected from the shell model [11]. The observation of a strong transition to the state at 13.5 MeV in $(p,p')$ is inconsistent with the $(n,p)$ reaction which locates no significant strength at 3.4 MeV in $^{20}$F. From the angular distributions between $\theta_{\mathrm{lab}}=3.0°$ to 10° Willis *et al.* obtain $B(\mathrm{GT})=0.185\pm0.023$ for the 11.26 MeV state. This value is somewhat larger than our value $B(\mathrm{GT})=0.161\pm0.029$ from the $(n,p)$ data. However, the $(p,p')$ and $(n,p)$ cross sections when compared at the same momentum transfers are in good agreement when the factor of 2 from the isospin Clebsch-Gordan coefficient for the projectile is taken into account. This suggests that different values of $\hat{\sigma}$ have been adopted to convert cross sections to $B$(GT). The $(n,p)$ results call into question the assignment of the states at 13.5 and 15.7 MeV as $T=1$, since these states should have been seen in the $^{20}$Ne$(n,p)^{20}$F reaction. Because of background from Kapton windows in the target the $^{20}$Ne$(p,p')$ reaction could not be observed above 17 MeV of excitation in $^{20}$Ne, so that predicted strong transitions to the 17.27 MeV state could not be seen.

The $^{20}$Ne$(p,n)^{20}$Na reaction has been studied at $E_p=160$ MeV [33] and $E_p=136$ MeV [13]. The energy resolution in the latter work was particularly good (340 keV FWHM) and we quote the GT strengths from the 136 MeV data in the following. For the transition to the 0.9 MeV state in $^{20}$Na, $B(\mathrm{GT})=0.161$ was obtained whereas the total strength from discrete states up to 10 MeV was $B(\mathrm{GT})=0.362$. If the GT strength found by a multipole decomposition of the total background is included, $B(\mathrm{GT})=0.472$, which is in good agreement with the $(n,p)$ data presented here. A summary of the GT strengths and quenching factors from the various measurements in mass-20 nuclei is given in Table IV.

TABLE IV. Comparison of GT strength extracted from $(n,p)$, from $(p,p')$ [11], $(p,n)$ [13], $(\pi^-,\gamma)$ [12] reactions for the analogs of the transitions to the 1.06 MeV state in $^{20}$F and for the total strength up to $E_x=10$ MeV.

| $E_x$ in $^{20}$F (MeV) | $B(\mathrm{GT}^+)$ $(n,p)$ | $B$(GT) $(p,p')$ | $B(\mathrm{GT}^-)$ $(p,n)$ | $B(\mathrm{GT}^+)$ $(\pi^-,\gamma)$ |
|---|---|---|---|---|
| 1.06 | 0.161±0.029 | 0.185±0.023 | 0.161 | 0.1607±0.030 |
| $\sum E_x=0-10.0$ | 0.585±0.209 | | 0.472 | |

## V. CONCLUSIONS

We have shown that relatively weak, low-lying GT strength can be extracted from $(n,p)$ reactions at intermediate energies using a high-pressure $^{20}$Ne gas target. Because of the approximate charge symmetry of nuclear forces similar GT strengths should be seen for analog transitions in $^{20}$F, $^{20}$Ne, and $^{20}$Na using the $(n,p)$, $(p,p')$, and $(p,n)$ reactions. The $B$(GT) values extracted for the discrete transitions to final states at 1 MeV in $^{20}$F and $^{20}$Na and at 11.26 MeV in $^{20}$Ne are in good agreement with the expectations from charge symmetry. The $(n,p)$ and $(p,p')$ cross sections to the analog states, at 200 MeV and for the same momentum transfer, are closely in agreement with the expected ratio of 1:2 although $B$(GT) values differing by 15% were extracted. This can be attributed to different values of the "unit cross section" $\hat{\sigma}$ used in the conversion from cross section to $B$(GT). The ratio $R(M1/\mathrm{GT})$ for this transition shows the dramatic effect of the spin-orbital interference in the $M1$ matrix element predicted by the shell model. The $M1$ strength for the 11.26 MeV transition obtained from 180° electron scattering is enhanced by nearly a factor of 5 relative to $M1$ strength expected from the spin part of the transition operator as determined by $B$(GT). The *sd* shell-model wave functions and free-nucleon operators describe this enhancement quantitatively.

The mass-20 data do not provide precise data on the quenching of GT strength relative to shell-model predictions. Since the GT strength is rather weak and distributed over a wide region of excitation, one has to rely on multipole decompositions which are plagued by large systematic uncertainties. The results from the multipole decompositions of our $(n,p)$ and of the 136 MeV $(p,n)$ data of Anderson *et al.* [13] are consistent with no quenching, whereas the GT strengths in discrete states observed in $(p,n)$ might indicate a small ($\sim$20%) quenching effect.

More definitive results on GT quenching are expected in nuclei near the middle of the *sd* shell where GT strength is stronger than in $^{20}$Ne, with a large fraction in a few strong transitions [13,34]. Furthermore, conclusions on MEC contributions to $M1$ from the ratio $R(M1/\mathrm{GT})$ can be drawn more readily for nuclei in the middle or upper half of the *sd* shell because orbital contributions are less important than in $^{20}$Ne. This has been shown [34] in mass 24 where accurate $M1$ distributions have recently become available. Nevertheless, the present work is a useful contribution to establish the systematics of GT quenching across the *sd* shell and for demonstrating the importance of spin-orbital interference in $M1$ transitions at the beginning of the *sd* shell.

*Present address: British Columbia Institute of Technology, Burnaby, British Columbia, Canada V5G 3H2.
†Present address: Ohio University, Athens, OH 45701.
‡Present address: Los Alamos National Laboratory, Los Alamos, NM 87545.
§Present address: Carleton University, Ottawa, Ontario, Canada K1S 5B6.

[1] T. N. Taddeucci, C. A. Goulding, T. A. Carey, R. C. Byrd, C. D. Goodman, C. Gaarde, J. Larsen, D. Horen, J. Rapaport, and E. Sugarbaker, Nucl. Phys. **A469**, 125 (1987).
[2] B. D. Anderson, T. Chittrakarn, A. R. Baldwin, C. Lebo, R. Madey, P. C. Tandy, J. W. Watson, C. C. Foster, B. A. Brown, and B. H. Wildenthal, Phys. Rev. C **36**, 2195 (1987).
[3] I. S. Towner, Phys. Rep. **155**, 263 (1987), and references therein.
[4] A. Arima, K. Shimizu, W. Bentz, and H. Hyuga, in *Advances in Nuclear Physics,* edited by J. W. Negele and E. W. Vogt, (Plenum, New York, 1987), Vol. 18, p. 1.
[5] B. H. Wildenthal, in *Progress in Particle and Nuclear Physics,* edited by D. H. Wilkinson (Pergamon, Oxford, 1984), Vol. 11, p. 5.
[6] B. A. Brown and B. H. Wildenthal, Nucl. Phys. **A474**, 290 (1987).
[7] B. A. Brown and B. H. Wildenthal, Annu. Rev. Nucl. Part. Sci. **38**, 29 (1988).
[8] W. L. Bendel, L. W. Fagg, S. K. Numrich, E. C. Jones, Jr., and H. F. Kaiser, Phys. Rev. C **3**, 1821 (1971).
[9] U. E. P. Berg, K. Ackermann, K. Bangert, R. Stock, and K. Weinhard, Phys. Rev. C **27**, 2987 (1983).
[10] U. E. P. Berg, K. Ackermann, K. Bangert, C. Bläsing, W. Naatz, M. K. Brussel, T. E. Chapuran, and B. H. Wildenthal, Phys. Lett. **140B**, 191 (1984).
[11] A. Willis, M. Morlet, N. Marty, C. Djalali, G. M. Crawley, A. Galonsky, V. Rotberg, and B. A. Brown, Nucl. Phys. **A464**, 315 (1987).
[12] C. J. Martoff *et al.*, Phys. Rev. Lett. **46**, 891 (1981).
[13] B. D. Anderson, N. Tamini, A. R. Baldwin, M. Elasaar, R. Madey, D. M. Manley, M. Mostajabodda'vati, J. W. Watson, W. M. Zhang, and C. C. Foster, Phys. Rev. C **43**, 50 (1991).
[14] R. L. Helmer, Can. J. Phys. **65**, 588 (1987).
[15] R. S. Henderson, B. W. Pointon, O. Häusser, A. Celler, R. L. Helmer, K. P. Jackson, B. W. Larson, C. A. Miller, and M. C. Vetterli, Nucl. Instrum. Methods **A286**, 41 (1989).
[16] MRS Manual, TRIUMF (unpublished).
[17] K. P. Jackson *et al.*, Phys. Lett. B **201**, 25 (1988).
[18] M. C. Vetterli *et al.*, Phys. Rev. C **40**, 559 (1989).
[19] J. Mildenberger *et al.*, Phys. Rev. C **42**, 732 (1990).
[20] A. Celler *et al.*, Phys. Rev. C **43**, 639 (1991).
[21] R. A. Arndt and L. D. Soper, Scattering Analysis Interactive Dial-in (SAID) program (SP88), unpublished.
[22] M. A. Moinester, Can. J. Phys. **65**, 660 (1987).
[23] R. Schaeffer and J. Raynal, Computer code DWBA70, extended version DW81, J. R. Comfort, Arizona State University, 1984 (unpublished).
[24] M. A. Franey and W. G. Love, Phys. Rev. C **31**, 488 (1985).
[25] K. H. Hicks, *et al.*, Phys. Rev. C **38**, 229 (1988).
[26] B. A. Brown, A. Etchegoyen, W. D. M. Rae, and N. S. Godwin, The Oxford-Buenos-Aires-MSU shell-model code (OXBASH), MSUCL Report No. 524, 1986.
[27] B. A. Brown, private communication.
[28] F. Ajzenberg-Selove, Nucl. Phys. **A475**, 117 (1987).
[29] C. Rangacharyulu, E. J. Ansaldo, D. Stockhausen, D. Bender, S. Müller, A. Richter, N. Lo Iudice, and F.

Palumbo, Phys. Rev. C **31**, 1656 (1985).
[30] W. P. Alford *et al.*, Nucl. Phys. **A514**, 49 (1990).
[31] G. F. Bertsch and I. Hamamoto, Phys. Rev. C **26**, 1323 (1982).
[32] O. Häusser *et al.*, to be published.
[33] J. Rapaport in *Fundamental Symmetries and Nuclear Structure,* edited by J. N. Ginocchio and S. P. Rosen (World Scientific, Singapore, 1989).
[34] A. Richter, A. Weiss, O. Häusser, and B. A. Brown, Phys. Rev. Lett. **65**, 2519 (1990).